Modeling of Saturn kilometric radiation arcs and equatorial shadow zone

Laurent Lamy, Philippe Zarka, Baptiste Cecconi, Sébastien L. G. Hess, Renée Prangé

Modeling of Saturn kilometric radiation arcs and equatorial shadow zone

L. Lamy,[1] P. Zarka,[1] B. Cecconi,[1] S. Hess,[1,2] and R. Prangé[1]

Received 6 June 2008; revised 9 August 2008; accepted 20 August 2008; published 28 October 2008.

[1] Accelerated electrons gyrating around Saturn's auroral (high latitude) magnetic field lines generate the intense Saturnian kilometric radiation (SKR). This radio emission is thought to be generated via the cyclotron maser instability (CMI) that predicts a strong anisotropy of the beaming pattern of the emission. Resulting visibility effects were suspected to be at the origin of characteristic features observed in Cassini's dynamic spectra as arc-shaped structures and shadow zones. By using the Planetary Radio Emissions Simulator (PRES) code, we model these visibility effects and their consequence on Cassini's observations of SKR: we compute the dynamic spectra resulting from the beaming pattern of CMI-generated SKR and its intersection with Cassini's trajectory. The SKR beaming pattern and its dependence on the frequency is computed for two typical electron distributions observed in auroral regions: a loss cone (favoring oblique emission) or a shell (favoring perpendicular emission). We successfully fit observed arc-shaped structures and shadow zones. Although oblique and perpendicular emissions both allow to produce radio arcs, the fit is better in the oblique case. Similarities and differences between observations and model results are discussed and perspectives are outlined.

Citation: Lamy, L., P. Zarka, B. Cecconi, S. Hess, and R. Prangé (2008), Modeling of Saturn kilometric radiation arcs and equatorial shadow zone, *J. Geophys. Res.*, *113*, A10213, doi:10.1029/2008JA013464.

1. Introduction

[2] Saturn is a source of intense nonthermal radio emission in the kilometric wavelength range, as discovered by the Voyager spacecraft in the 1980s. The average properties of the Saturn kilometric radiation (SKR) deduced from early studies [*Kaiser et al.*, 1984, and references therein] have recently been confirmed and expanded by *Lamy et al.* [2008] via the analysis of several years of quasi-continuous observations recorded by the High Frequency Receiver (HFR) of the Radio and Plasma Wave Science (RPWS) instrument onboard the Cassini spacecraft in orbit around Saturn [*Gurnett et al.*, 2004]. The kilometric radio sources are confined to auroral regions with latitudes $\geq 70°$. The SKR is emitted in the 10–1200 kHz frequency range, peaking at 100–400 kHz. The emission has a high degree of circular polarization with a sense related to the hemisphere of origin: northern and southern sources emit right-handed (RH) and left-handed (LH), respectively, polarized radiation, consistent with emission on the extraordinary (X) mode. In typical SKR spectra, the RH component generally dominates above 600 kHz, whereas the LH component is more intense below that frequency.

[3] Voyager observations showed that SKR sources do not corotate with the planet but are rather fixed in local time (LT) approximately in the dawn-to-noon sector [*Warwick et al.*, 1981; *Galopeau et al.*, 1995]. *Boischot et al.* [1981] noticed that the SKR is often organized in arc-shaped structures in the time-frequency (t, f) plane, similar to those observed for the Jovian decametric emissions. These arcs are well visible in Cassini/RPWS dynamic spectra (Figure 1a) and often reveal a double structure where both nested arcs display an opposite sense of polarization (Figure 1b). Cassini observations also confirmed the existence of an equatorial shadow zone (ESZ), and constrained its equatorial extent. This one is frequency-dependent. It is minimum for the SKR peak frequencies ($\sim$4 R_S at 200 kHz), and it increases at high and low frequencies ($\sim$6–7 R_S at 80 and 900 kHz) on both sides of the SKR spectrum.

[4] The SKR is believed to be emitted via the cyclotron maser instability (CMI), dominantly on the X mode at nearly its cutoff frequency f_X, itself close to the local electron gyrofrequency f_{ce} in the source [*Wu*, 1985; *Galopeau et al.*, 1989; *Zarka*, 1998]. The CMI theory predicts that the resulting radio emission is beamed within a thin hollow cone whose axis is aligned with the local magnetic field line and which exhibits a wide opening (large aperture angle) θ. *Lamy et al.* [2008] estimated the beaming angle to $\theta \leq 70°$ at the SKR peak (f $\sim$ 200 kHz). They suggested that the strong anisotropy of the emission could be responsible for SKR time-frequency structures and shadow zones. This is quantitatively investigated in the present paper.

[1] LESIA, Observatoire de Paris, CNRS, UPMC, Université Paris Diderot, Meudon, France.
[2] LUTH, Observatoire de Paris, CNRS, UPMC, Meudon, France.

0148-0227/08/2008JA013464

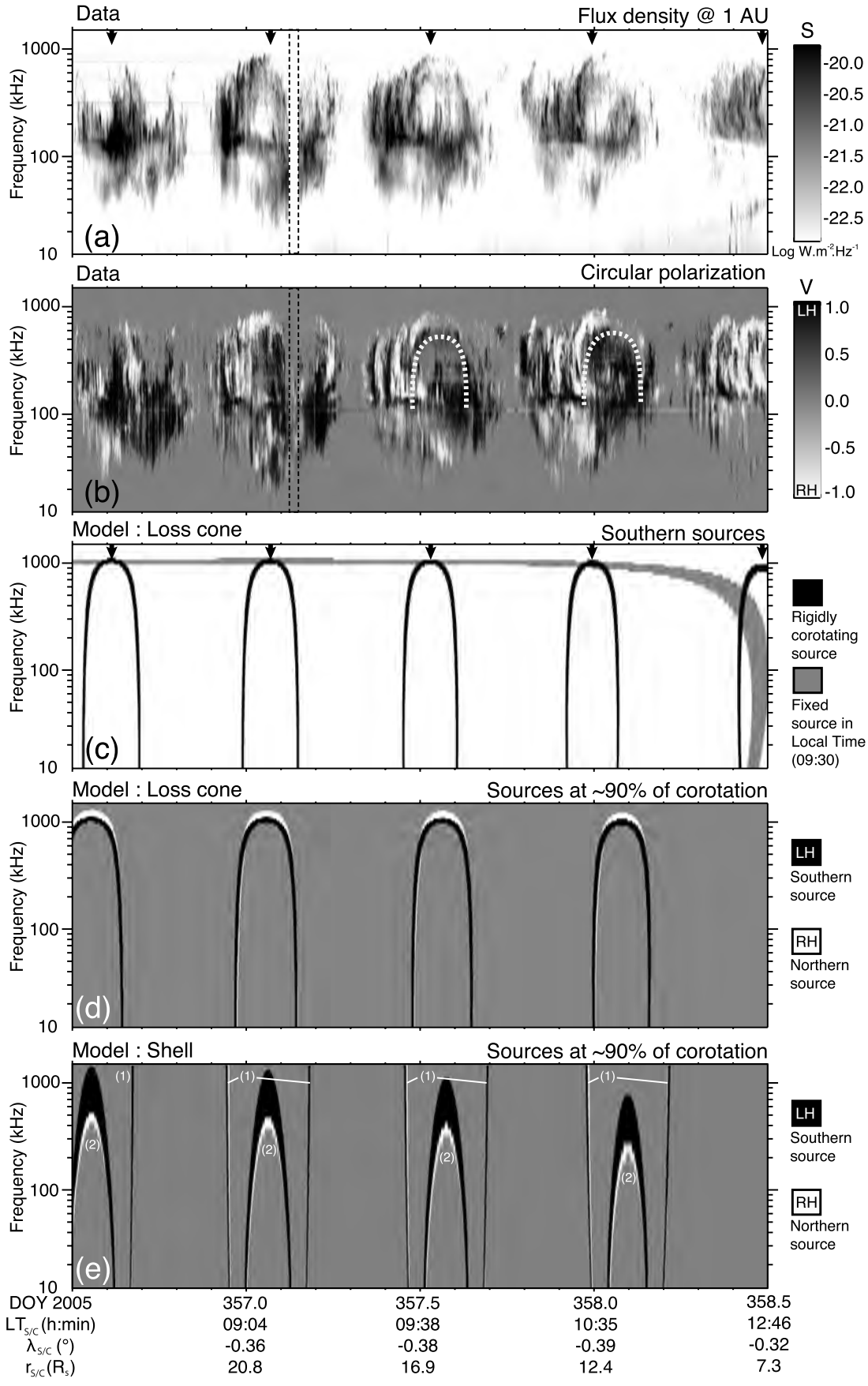
Data
Flux density @ 1 AU
S
-20.0
-20.5
-21.0
-21.5
-22.0
-22.5
Log W.m-2.Hz-1
Frequency (kHz)
1000
100
10
(a)
Data
Circular polarization
V
LH
RH
1.0
0.5
0.0
-0.5
-1.0
(b)
Model : Loss cone
Southern sources
Rigidly corotating source
Fixed source in Local Time (09:30)
(c)
Model : Loss cone
Sources at ~90% of corotation
LH
Southern source
RH
Northern source
(d)
Model : Shell
Sources at ~90% of corotation
(1)
(2)
LH
Southern source
RH
Northern source
(e)
DOY 2005 357.0 357.5 358.0 358.5
LTS/C (h:min) 09:04 09:38 10:35 12:46
λS/C (°) -0.36 -0.38 -0.39 -0.32
rS/C (Rs) 20.8 16.9 12.4 7.3

Figure 1

[5] Moreover, similar to auroral radio emissions at Earth and Jupiter, the SKR appears to be associated with ultraviolet (UV) aurorae due to the precipitation into the atmosphere of accelerated electrons with energies in the range ~1–20 keV [*Cowley et al.*, 2004a, 2004b]. In quiet magnetospheric conditions, the (southern) auroral oval typically lies between −70° and −75° [*Badman et al.*, 2006, and references therein], at an estimated altitude of 1000 km above the 1-bar level [*Gérard et al.*, 2004]. UV auroral patterns as well as isolated structures have been observed to subcorotate at a rate between 30% to 75% of the planetary rotation rate (which is about 10 h 45 min) [*Clarke et al.*, 2005; *Grodent et al.*, 2005].

[6] An early attempt to model kronian arc shapes was performed by *Thieman and Goldstein* [1981] using an empirical form of the radio beaming angle $\theta(f)$, which was found to lie in the range 75°–85°. Assuming saturation of the CMI by trapping of energetic electrons in the wave electric field, *Galopeau et al.* [1989] found an abrupt decrease of the beaming angle at high frequencies (i.e., the emission cone closes). Recently, *Hess et al.* [2008] developed the PRES code (Planetary Radio Emissions Simulator) with which they successfully modeled observations of Io-Jupiter arcs. Assuming a radio source beaming pattern constrained by CMI physics, PRES allows to compute the dynamic spectra resulting from geometrical visibility effects for any magnetized planet.

[7] Here, we present modeling of the SKR double arc-shaped structures and equatorial shadow zone observed by Cassini from low latitudes. The model and typical emission parameters are discussed in section 2. Simulations results for double arcs and ESZ are presented in sections 3 and 4. Results and perspectives are discussed in section 5.

2. Model of Kronian Radio Emissions

2.1. CMI and Electron Distributions

[8] The PRES code is based on the CMI, that is the best candidate generation mechanism for auroral radio emissions of all magnetized planets. For Saturn's magnetic field, we use the SPV model for the internal magnetic field component [*Davis and Smith*, 1990] and the *Connerney et al.* [1983] model of Saturn's ring current. CMI basics and its driving unstable electron distributions have been described in detail by *Hess et al.* [2008] and are only briefly recalled here. It is a resonant interaction between energetic (a few keV) electrons gyrating along high latitudes magnetic field lines (of gyropulsation ω_{ce}) and circularly polarized electromagnetic waves (of pulsation ω). The resonance equation writes

$$\omega = \frac{\omega_{ce}}{\Gamma} + k_{//} v_{//} \tag{1}$$

where Γ is the relativistic Lorentz factor and $k_{//}$ and $v_{//}$ are the projection of the wave **k** vector and the electron velocity onto the direction of the magnetic field at the source [*Wu and Lee*, 1979; *Wu*, 1985].

[9] Here we study the dominant emission, generated on the X mode near its cutoff ω_X. As SKR sources likely lie in depleted plasma regions ($\omega_{pe} \ll \omega_{ce}$, where ω_{pe} is the plasma frequency [see *Galopeau et al.*, 1989]), we hereafter make the approximation $\omega \sim \omega_X \sim \omega_{ce}$. We also assume refraction effects to be negligible along the raypath, implying a refraction index $N \sim 1$ (N is given by the Appleton-Hartree cold plasma dispersion equation) and consequently straight-line propagation from the source to the observer.

[10] The CMI amplifies radio waves at the expense of the energetic electrons perpendicular energy. This free energy may come from a loss cone or a shell distribution [see *Treumann*, 2006; *Hess et al.*, 2008]. Both cases are investigated here. A loss cone is obtained in the upgoing (magnetically mirrored) electrons distribution when part of the downgoing electrons are lost by collisions in the atmosphere. This type of distribution favors oblique radio emission [*Galopeau et al.*, 2004]. The spectral variation of the radio beaming angle $\theta(f)$ with respect to the local magnetic field line then writes

$$\theta = \arccos\left(\frac{v_{e-}}{c}\frac{1}{N}\frac{\omega_{ce}}{\omega}\frac{1}{\sqrt{1-\omega_{ce}/\omega_{ce,\max}}}\right) \tag{2}$$

where N is the refraction index, v_{e-} is the characteristic velocity of resonant electrons, and $\omega_{ce,\max}$ is the maximum gyropulsation at the field line atmospheric footprint.

[11] In the frame of the above assumptions ($\omega \sim \omega_{ce}$ and $N \sim 1$), equation (2) reduces to

$$\theta = \arccos\left(\frac{v_{e-}}{c}\frac{1}{\sqrt{1-\omega_{ce}/\omega_{ce,\max}}}\right) \tag{3}$$

On the other hand, a shell distribution results from the adiabatic evolution of electron beams. It favors perpendi-

Figure 1. Observed and simulated SKR dynamic spectra during 2 days of year 2005. (a) and (b) SKR flux density S normalized to 1 AU and the normalized degree of circular polarization V (black for LH, white for RH), respectively. Dashed lines mark data gaps and arrows indicate the SKR rotational modulation. Yellow dotted lines highlight the thin double arcs discussed in section 3. (c) Simulated spectrum for two southern sources (each made of point sources aligned along a single magnetic field line, whose footprint latitude is $\lambda_B = -70°$, distributed in altitudes according to the electron gyrofrequency in the range [10,1200 kHz], see Table 1), and for a beaming angle $\theta(f)$ computed with a loss cone electron distribution (see equation (3)). The grey arc results from a source fixed in LT at 0930 (belonging to the LT range swept by Cassini). The black arcs result from consecutive passes of a source fixed in longitude (i.e., in corotation with the planet) in front of the observer. (d) Simulated spectrum produced by the same loss-cone-driven conjugate southern and northern sources moving at ~90% of the corotation rate. As in Figure 1b, southern sources are plotted in black and northern ones in white. (e) Spectrum produced by the same sources for shell-driven simulations and two different constant values of $\theta(f)$. The (1) and (2) refer to $\theta(f) = 90°$ (perpendicular emission) and $\theta(f) = 55°$ (oblique emission), respectively. See color version of this figure in the HTML.

Table 1. Typical Sets (and Ranges) of Parameters Used in the Simulations

Radio Source Footprint Latitude λ_B	Radio Source Longitude	Aurora's Altitude (km)	Electron Distribution	Electron Velocity v_{e-} (Kinetic Energy)	Beaming Angle θ	Cone Thickness $\Delta\theta$	Observer's Location	Frequency Range (kHz)	Time Step (min)
$-70°$	0°–360°	1000	Loss cone	0.3 c (23 keV)	see equation (3)	5°	Cassini	10–1200	3
($-65°$ to $-80°$)				(0.06–0.3 c (1–23 keV))		(1–5°)			
$-70°$	0°–360°	-	Shell	-	55°	5°	Cassini	10–1200	3
($-65°$ to $-80°$)					(55°–90°)	(1–5°)			

cular radio emission, thus, in this case, $\theta(f)$ is constant and in principle ~90°.

[12] For both distributions, the actual beaming angle may be lower (by several degrees or even tens of degrees) than the above $\theta(f)$ because of possible refraction effects at the edges of cold plasma depleted cavities surrounding radio sources as in the Earth's case [*Louarn and Le Quéau*, 1996]. Note, however, that we do not have any evidence of the existence of such cavities at Saturn.

2.2. Simulation Parameters

[13] The PRES code computes the geometrical visibility of selected radio sources for a given observer. Comparing the direction of the observer relative to the magnetic field vector at every point source with its predicted emission pattern, it merely determines whether the observer (here Cassini) detects (is in the beam of) or not (is not in the beam of) radio sources, and then generates a simulated dynamic spectrum. We have performed a parametric study and compared it to observational data. The parameters used in the following simulations and parametric studies are listed in Table 1.

[14] Magnetic field lines along which radio sources are distributed are defined by the coordinates of their footprint at the planetary surface. The footprint longitude has been investigated within the whole 0°–360° range, whereas the footprint latitude, hereafter noted λ_B, has been studied within the typical range of UV aurorae determined for the (most observed) southern oval (i.e., $-65°$ to $-80°$). Southern and/or northern parts of each field line are individually populated by radio sources whose altitude range is defined by the typical SKR frequency range ~10–1200 kHz (with the assumption $f = f_{ce}$). Hereafter we simply call "source" the distribution of individual radio sources (or point sources) within this frequency range along a single field line in one hemisphere. Each individual radio source emits waves propagating in straight lines along a thin hollow conical sheet defined by its aperture angle $\theta(f)$ (see section 2) and its sheet thickness $\Delta\theta$. The emission pattern is thus defined by $\theta(f) \pm \Delta\theta/2$.

[15] As mentioned above, the difference between loss cone and shell driven emissions only lies in the beaming angle, $\theta(f)$, which is constant in the shell case whatever the frequency or the resonant electron velocity. Following equation (3), the loss cone driven beaming angle depends on the resonant electron velocity and on $\omega_{ce,\max}$. The latter corresponds to the maximal pulsation reached at the atmospheric limit where aurorae can occur. It has been computed using the typical altitude of 1000 km found for the UV aurorae [*Gérard et al.*, 2004]. Because of the 0.04 R_S northward offset of the kronian magnetic dipole, the resulting maximum frequency ($f_{ce,\max} = \omega_{ce,\max}/2\pi$) is different in the two hemispheres (for a magnetic field line with $\lambda_B = -70°$: $f_{ce,\max} \sim 1500$ kHz in the southern hemisphere and $f_{ce,\max} \sim 1840$ kHz in the northern one). Then $\theta(f)$ depends on the electron velocity, for which a large range of values is explored (~$0.06-0.3c$ with c being the velocity of light).

[16] The observer's location is directly given by Cassini's ephemeris.

[17] Within this set of parameters, the source latitude and longitude, as well as the cone parameters $\theta(f)$ (related to the electron velocity in the loss cone case) and $\Delta\theta$ are poorly constrained. Appendix A, which presents simple simulations of radio sources moving with respect to a circular orbiter, displays a parametric study investigating the influence of those parameters. As each of them strongly affects the visibility of the emissions, our aim is to constrain them by comparing observed and simulated dynamic spectral features.

3. Arc-Shaped Structures

[18] Arc-shaped structures in the (t, f) plane, discovered by Voyager [*Boischot et al.*, 1981], are also observed by Cassini. Figures 1a and 1b display typical dynamic spectrum of SKR including thin arcs detected when Cassini is located at low latitudes. They often reoccur with remarkable morphological similarity, as for the examples marked with yellow dotted lines on Figure 1b. This suggests that they could result from a single source observed twice. Moreover, the arc-shaped structure appears to shift relative to the overall SKR modulation pattern attributed to planetary rotation (here indicated by arrows) with a recurrence period of ~90% of this rotation rate. On Figures 1a and 1b we also noticed that each marked arc is actually double, with nested components displaying opposite senses of circular polarization (this is quite clear above 400 kHz). Figure 1b shows that the RH component is slightly shifted toward higher frequencies relative to the LH one, consistent with Saturn's magnetic field offset and/or the existence of a magnetic anomaly. This latter point was already noted by *Lamy et al.* [2008] to be a systematic trend for observations from the neighborhood of the equator.

[19] Figures 1c and 1d display results of PRES simulations using a beaming angle determined by loss-cone-driven CMI for a source distributed along a single field line and input parameters listed in Table 1 that provide the best qualitative agreement with observations (see section 5).

[20] Figure 1c displays the two limiting cases for a southern source moving with respect to Cassini: the single grey arc corresponds to a source fixed in LT (as suggested by Voyager studies), whereas the black arcs correspond to a

Table 2. Influence of Footprint Latitude λ_B and Electron Velocity v_{e-} on the Maximum Frequency of Arcs Simulated With Loss-Cone-Driven CMI for Northern and Southern Conjugate Sources[a]

	v_{e-}			
λ_B	0.1 c	0.2 c	0.3 c	0.4 c
−65°	RH > 1500	RH:1500	RH:1300	RH:1000
	LH:1250	LH:1250	LH:1100	LH:900
−70°	RH > 1500	RH:1500	RH:1100	RH:750
	LH:1400	LH:1250	LH:1000	LH:700
−75°	RH > 1500	RH:1250	RH:650	RH:250
	LH:1450	LH:1100	LH:650	LH:300

[a]Footprint latitude λ_B is one of the field line supporting the source, and maximum frequency is expressed in kHz. RH, northern; LH, southern. Since the observed maximum frequency may vary with time (with location of Cassini), values of f_{max} are listed for the specific arc at day 357.5 of year 2005 on Figure 1. To provide precise estimations of the maximal detected frequency, the source frequency range has been extended from [10,1200 kHz] (see Table 1) to [10,1500 kHz].

source fixed in longitude (i.e., in rigid corotation with the planet) observed several time in phase with the main SKR bursts (arrowed). Those simulations illustrate that an arc-shaped structure in the (t, f) plane is obtained when a single source sweeps by the observer. Both types of arcs display the same maximum frequency around 1000 kHz, close to that of the observed arcs in Figure 1a, but they do not correctly reproduce neither the observed temporal width nor the recurrence period. Nevertheless, regarding the latter characteristics, the black arcs qualitatively resemble the observed ones, whereas the grey arc does not. The parametric study displayed in Appendix A investigates the dependence of the simulated arc morphology (in term of shape, temporal width and thickness and maximum frequency) with respect to input parameters. Table 2 quantitatively illustrates the strong influence of the pair of parameters (footprint latitude, electron velocity) on the maximum observed frequency of simulated arcs at a given time. The pair ($\lambda_B = -70°$, $v_{e-} = 0.3$ c) provides the best fit to the observations. The temporal width and the recurrence period of simulated arcs are directly related to the velocity of the source with respect to the observer.

[21] Figure 1d simulates a dynamic spectrum obtained with a southern source at ∼90% of rigid corotation. The modeled arcs display a temporal width (expanded relative to Figure 1c) in good agreement with individual arcs of Figures 1a and 1b. Moreover, this level of subcorotation provides the right phase of observed recurrent arcs, making plausible the observation of a single subcorotating source observed at least twice (other arc structures of Figures 1a and 1b are roughly in phase with modeled arcs). This agreement allows to investigate the cone thickness that directly affects the instantaneous duration (i.e., temporal thickness) of simulated arcs. Following the parametric study of Appendix A, we can determine that $\Delta\theta \sim 5°$. Figure 1d also displays RH arcs from a northern source conjugate to the southern one and thus at the same subcorotation level. We obtain a well-defined modeled double arc structure in which the RH component is shifted toward higher frequencies relative to the LH one, consistent with Figures 1a and 1b.

[22] For comparison, PRES simulations based on the shell-driven CMI are displayed on Figure 1e for two different values of $\theta(f) = 90°$ (indicated by a (1)) and 55° (indicated by a (2)) and inputs parameters listed in Table 1. Only the oblique emission leads to modeled arcs resembling those observed: for $\theta(f) = 55°$, we obtain arcs with the appropriate shape still with $\lambda_B = -70°$. But this beaming angle largely differs the one predicted for perpendicular emission (90°), and would thus imply strong refraction at the source. Further, shell-modeled arcs show a large variation of their maximum frequency with the observer's position (by several hundreds of kHz over the time interval of Figure 1), and their double structure systematically displays the LH arc above the RH one, contrary to the observations.

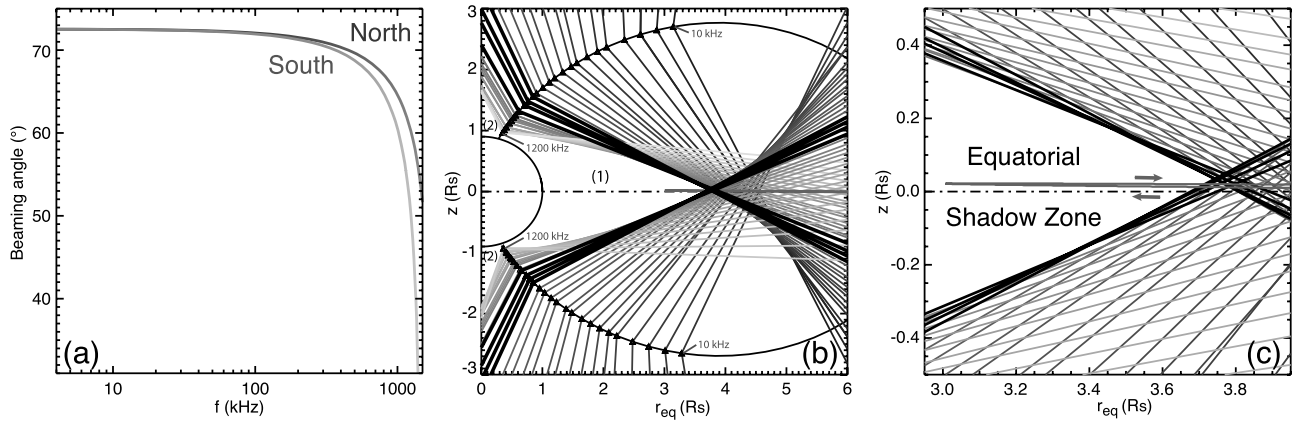

Figure 2. (a) Loss-cone-driven beaming angle $\theta(f)$ (see equation (3)) computed in both hemispheres along the field line defined by $\lambda_B = -70°$, for an altitude of the aurora of 1000 km and a resonant electron velocity set to 0.3 c (see Table 1). The abscissa extend from 4 to 1500 kHz; θ_{north} and θ_{south} are displayed in blue and red, respectively. (b) Meridian cross section of emission cones for northern and southern SKR sources (triangles) emitting between 10 and 1200 kHz along the magnetic field line defined by $\lambda_B = -70°$. Black lines correspond to emission cones for frequencies between 200 and 400 kHz. The (1) and (2) indicate the equatorial and polar shadow zones. (c) A zoom of Figure 2b. The green line shows the projected Cassini trajectory for the time interval of Figure 3a. See color version of this figure in the HTML.

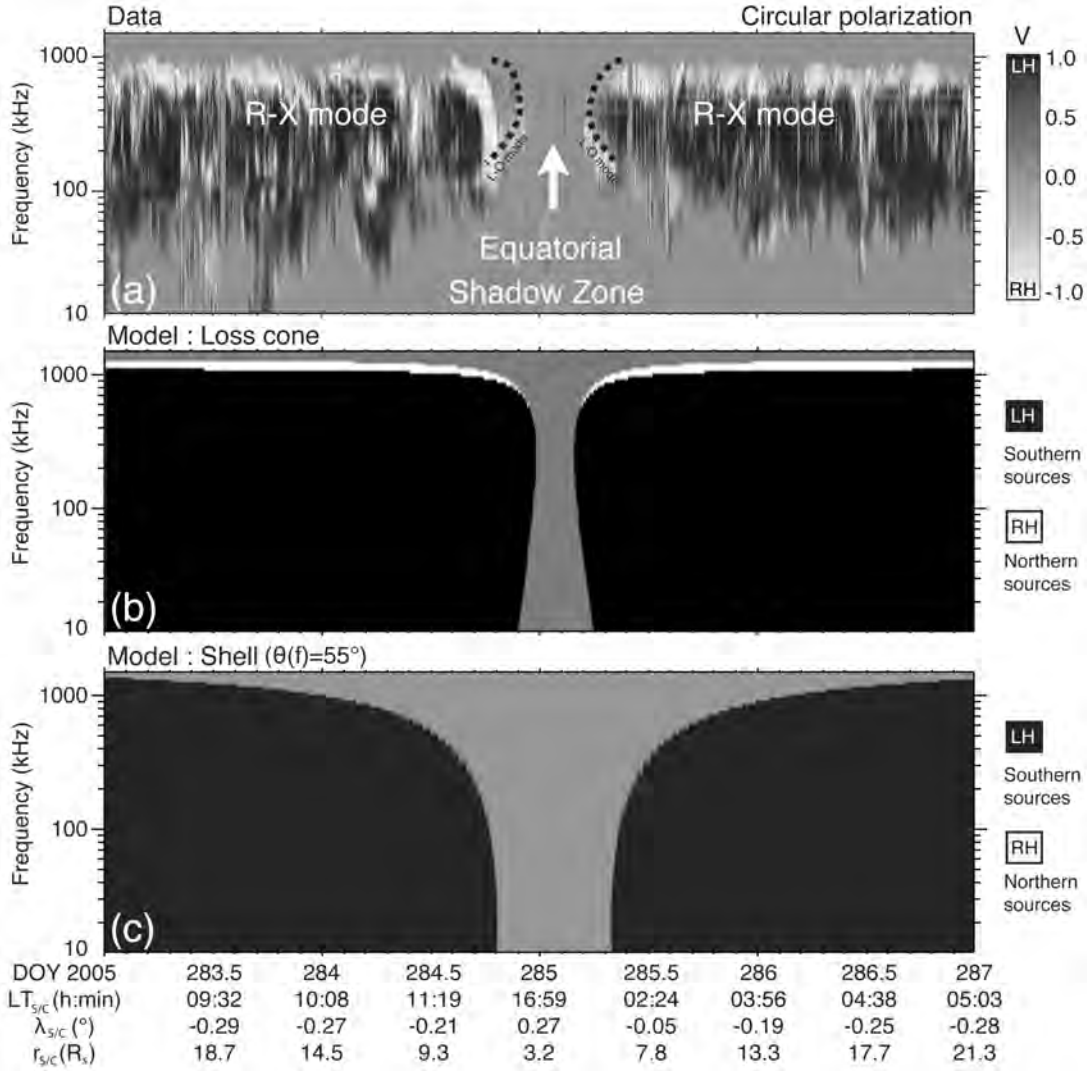

Figure 3. (a) Observed dynamic spectrum of SKR circular polarization degree during a crossing of the ESZ (adapted from Figure 6a of *Lamy et al.* [2008]). (b) Simulated dynamic spectrum under the assumption of a loss-cone-driven CMI generation of southern (black) and northern (white) sources distributed at all LT around the planet (with a 30 s temporal resolution) on magnetic field lines defined by $\lambda_B = -70°$. Regions of the (t, f) plane which are simultaneously illuminated by the RH and LH components are plotted in black in order to take the predominance of the LH emission into account. (c) Same as Figure 3b for shell-driven simulations using $\theta(f) = 55°$. In this case, the RH component is systematically masked by the LH one.

[23] The latter point allows to discriminate between loss-cone-driven and shell-driven arcs. As the shell-driven case implies constant $\theta(f)$, the geometrical visibility of RH and LH components is symmetrical with respect to the magnetic equatorial plane. However, for an observer located in the kronographic equatorial (rings) plane, the magnetic field northward offset induces an asymmetry which leads to the observation of double arcs with LH (southern) emissions observed at higher frequencies. In the loss-cone-driven case, $\theta(f)$ depends on $\omega_{ce,\max}$, which itself differs in both hemispheres (see section 2). As displayed in Figure 2a, $\theta_{\text{south}}(f)$ falls more abruptly than $\theta_{\text{north}}(f)$ at high frequencies. The resulting geometrical effect on the visibility in the equatorial plane competes with the previous trend and favors the observation of RH emission at higher frequencies.

4. Equatorial Shadow Zone

[24] Another important consequence of the anisotropy of the SKR beaming is the existence of regions of space which are never illuminated by any SKR beam. Figure 3a displays a typical example of SKR disappearance when Cassini crosses the ESZ. Again, the LH polarization dominates the dynamic spectrum below 600 kHz and the RH one above 600 kHz. The extent of the ESZ is frequency-dependent: it is minimum at $\sim$4 R_S for $f = 200-400$ kHz, and up to 6–7 R_S at 80 and 900 kHz, as sketched by the dashed black lines on Figure 3a. Note that the RH

component observed just around ESZ below ~300 kHz is attributed to ordinary (O) mode emission (B. Cecconi et al., Goniopolarimetry of the Rev. 29 perikrone using the Cassini/RPWS/HFR radio receiver, submitted to *Journal of Geophysical Research*, 2008). We must consequently not take this emission into account when comparing simulation and observations.

[25] Figures 3b and 3c display loss-cone- and shell-driven simulations, respectively, performed with the same parameters as above (see Table 1), except that southern and northern sources are now distributed at all longitudes. The LH component is assumed to dominate when both components are detected simultaneously. The simulated dynamic spectrum shows a very good qualitative agreement with the data for (and only for) the loss-cone-driven emission (Figure 3b): RH predominates at the highest frequencies and the extinction of the signal indeed occurs around DOY 285.0 as observed. Its duration precisely fits the one of the observed extinction. The disappearance/reappearance of the emission displays a similar frequency dependence with a minimum ESZ extent observed at f = 200–400 kHz. In Figures 2b and 2c, the emission cones which correspond to point sources emitting between 200 and 400 kHz are plotted in black. They clearly determine the minimum ESZ extent at ~3.75 R_S (in the magnetic equatorial plane, thus at slightly northern latitude), consistent with the observations. This model based on a loss-cone-driven beaming angle also predicts the existence of polar shadow zones very close to the planet (below ~1.5 R_S, see zones labeled 2 in Figure 2b).

[26] Another modeled feature in Figure 3b is consistent with observations of Figure 3a: around ESZ crossing, the X mode RH emission (above 300–400 kHz, excluding thus O mode RH SKR) disappears before and reappears after the LH one. In other words, the LH component is observed closer to the planet. This is especially clear at reappearance (at disappearance, the LH emission is more sporadic and somewhat hides this effect). As illustrated by Figure 2c, this is due to the asymmetric visibility of both components along Cassini's near-equatorial trajectory (green line).

[27] As in the case of Figures 1c and 1d, in spite of a good qualitative match, the modeled high-frequency limit of the emission around ESZ slightly differs from the observed one (see also Table 2), whereas the low-frequency range (below ~100 kHz) is poorly modeled. This is discussed in section 5.

5. Discussion

[28] Modeling of SKR (t, f) features observed by Cassini from low latitudes have revealed that (1) observed arc-shaped structures are consistent with CMI-driven radio emissions from sources moving with respect to the observer; (2) such arcs do not originate from SKR sources fixed in LT, but rather from subcorotating sources (here at ~90% of corotation); (3) the observed double arc structure is correctly simulated (RH arc at higher frequencies than the LH one) when using a beaming angle determined by loss-cone-driven CMI; and (4) loss cone simulations of ESZ crossing are also consistent with data regarding the time of extinction, its approximate shape and size in the (t, f) plane (corresponding to a minimum ESZ equatorial extent at f = 200–400 kHz), and the disappearance of RH emission at larger distances than for LH emissions (when observing from near the equator).

[29] Results 1 and 2 recall the subcorotation observed for UV auroral sources [*Clarke et al.*, 2005]. More SKR arcs should be modeled for being able to obtain statistical results, but this first result confirms that SKR can be observed from a large range of LT, not restricted to the dawn-to-noon sector. This is not inconsistent with the fact that SKR (and UV aurora) is more active in the morning side, but suggests that although the emission can be produced in a broad range of LT, its intensity is enhanced when the source is located in the morning sector [*Lamy et al.*, 2008; *Farrell et al.*, 2005].

[30] In our model, the details of simulated arc shape, maximum frequency, and ESZ extent, are strongly sensitive to two key parameters: the footprint latitude of the magnetic field line hosting the source and the beaming angle variation along the field line (i.e., with frequency). A typical value of $\lambda_B = -70°$, as deduced here, is consistent with that of the footprint latitude of quiet southern UV aurorae [*Badman et al.*, 2006, and references therein]. Then, according to results 3 and 4, best fits are obtained with $\theta(f)$ decreasing from ~70° to ~40° with increasing frequency, the shape of this decrease being different in the two hemispheres and consistent with the radio beaming predicted by loss-cone-driven CMI. However, the kinetic energy of emitting electrons must be $\geq$ 23 keV ($v_{e-} \geq 0.3c$, see Table 2) in order to get low enough values of $\theta(f)$, and accordingly low enough values of the maximum SKR frequency (observed at ~800 kHz). This is at the upper end of previous estimates based on other types of observations and modeling. Typical energies of precipitating auroral electron inferred from UV studies are in the range 10 to 20 keV [*Cowley et al.*, 2004a, 2004b]. Much higher energies are also difficult to invoke for SKR generation, with the reminder that *Galopeau et al.* [1989] successfully modeled the SKR spectrum using 1–10 keV electrons. Thus, If realistic electron kinetic energy ($\leq$ 20 keV) does not allow to compute low enough values of $\theta(f)$, leading to best simulations of SKR features, additional causes should be searched for (see below).

[31] In these first simulations, we have neglected refraction effects. They can intervene in two ways: first, a refraction index $N \neq 1$ at the source implies a modification of the variation of the loss-cone-driven beaming angle $\theta(f)$, following equation (2); second, the apparent beaming angle of the radiation exiting the source may be affected by multiple refractions/reflections at the edges of the source region if this source is a plasma cavity as in the case of Earth [see *Louarn and Le Quéau*, 1996]. The latter effect may apply to both loss-cone- and shell-driven CMI, and should lead to lower $\theta(f)$. However, as previously mentioned, there is no evidence for the existence of such cavities until now. In addition, refraction should significantly affect the raypath of low-frequency emissions (typically below ~100 kHz) propagating in the complex low-latitude plasma environment of Saturn (see, e.g., the plasma models of *Galopeau et al.* [1989] and *Persoon et al.* [2006]). Similar to the deviation of auroral radio waves at Earth by the plasmasphere [*Hashimoto*, 1984; *Xiao et al.*, 2007, and references therein], refraction along the raypath should also result in lower apparent values of $\theta(f)$. This effect could explain the difference between modeled and observed dynamic spectra at low frequencies. It deserves a dedicated ray-tracing study, beyond the scope of this paper. Finally, a

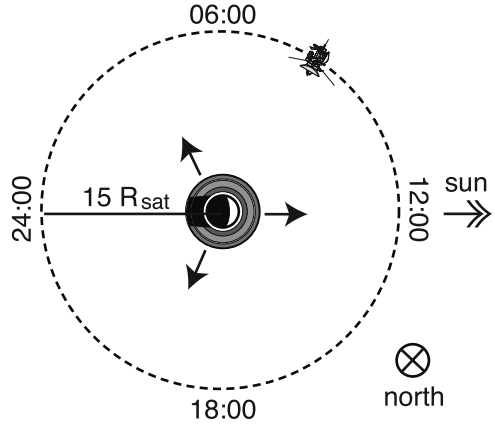

Figure A1. Schematic geometrical configuration for a spacecraft on a circular orbit at 15 R_S in the equatorial plane, observing southern radio sources defined by $\lambda_B = -70°$ and LT = 0400, 1200, and 2000 (black arrows). Results of simulations of both loss-cone- and shell-driven emissions are displayed in Figures A2 and A3.

seasonal effect implying a difference in the plasma density (and thus of the refraction index N) between both hemispheres might also lead to differences in LH and RH beaming (and thus in dynamic spectra).

[32] Our simulations of SKR arcs imply a cone thickness of 5°. This value is comparable to average values measured for Jupiter's hectometer and decameter radio emissions [*Zarka et al.*, 2004] and slightly larger than instantaneous observed/modeled values [*Kaiser et al.*, 2000; *Queinnec and Zarka*, 1998; *Hess et al.*, 2008]. It must be noted that effective arc thickness is actually the convolution of the cone thickness of a point source with the spatial distribution (versus latitude,longitude) of sources of equal frequency. We may thus obtain similar arc simulations with a narrower cone but a more extended source (here we assumed a point source).

[33] The first published goniopolarimetric analysis of SKR (including **k** vector determination and thus direct source localization) (B. Cecconi et al., submitted manuscript, 2008) shows that southern radio sources are distributed along magnetic field lines with footprints between −80° and −65°, with a typical extension of a few degrees. The authors also computed the observed beaming angle, found to decrease with the frequency from ∼65° to ∼50° in the northern hemisphere, and from ∼55° to ∼40° in the southern hemisphere. A statistical goniopolarimetric analysis of SKR should allow to better define the input parameters of our PRES modeling (source footprint latitude and

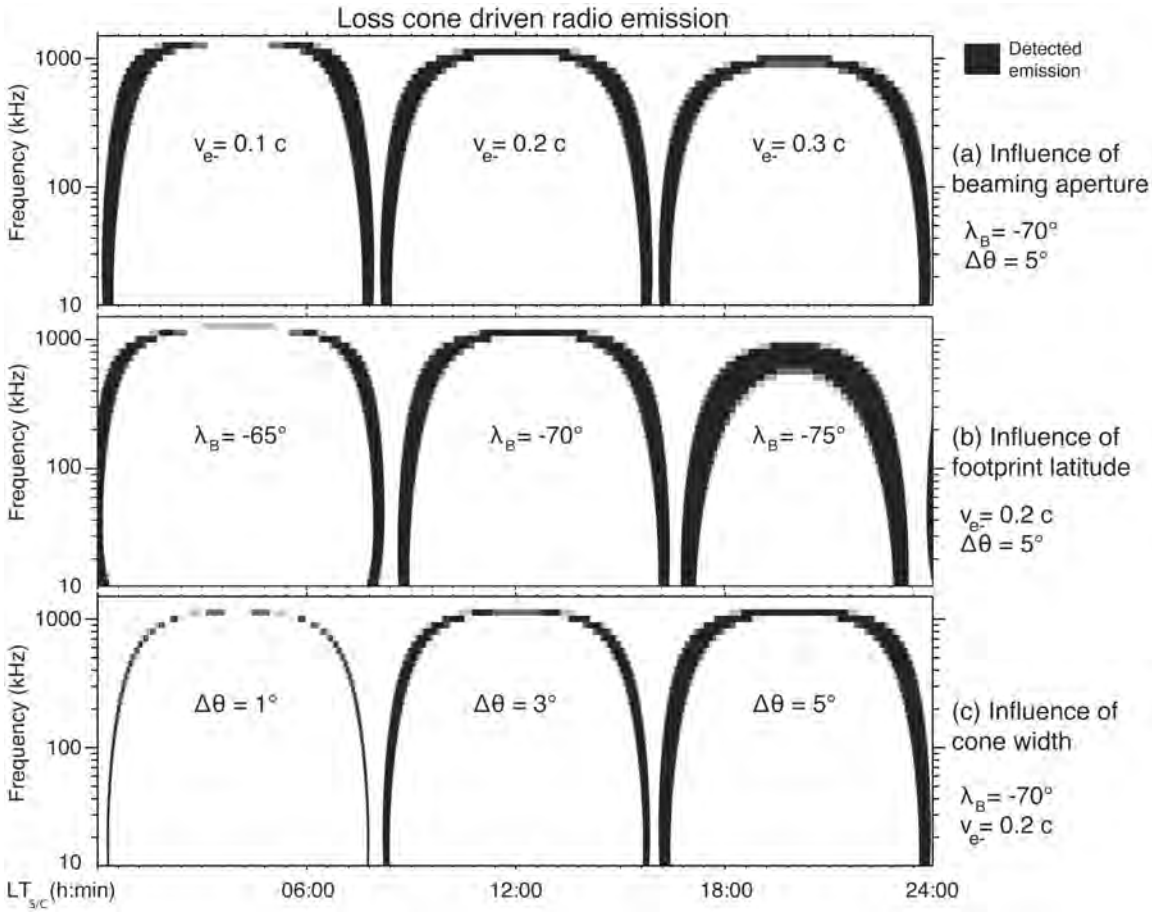

Figure A2. Simulated dynamic spectra of loss-cone-driven emissions for a spacecraft in circular orbit as defined in Figure A1. The abscissa gives the spacecraft LT. (a), (b), and (c) The influence of the free parameters $\theta(f)$ (related to v_{e-}, see equation (3)), λ_B, and $\Delta\theta$, respectively. Arcs are successfully simulated in all cases.

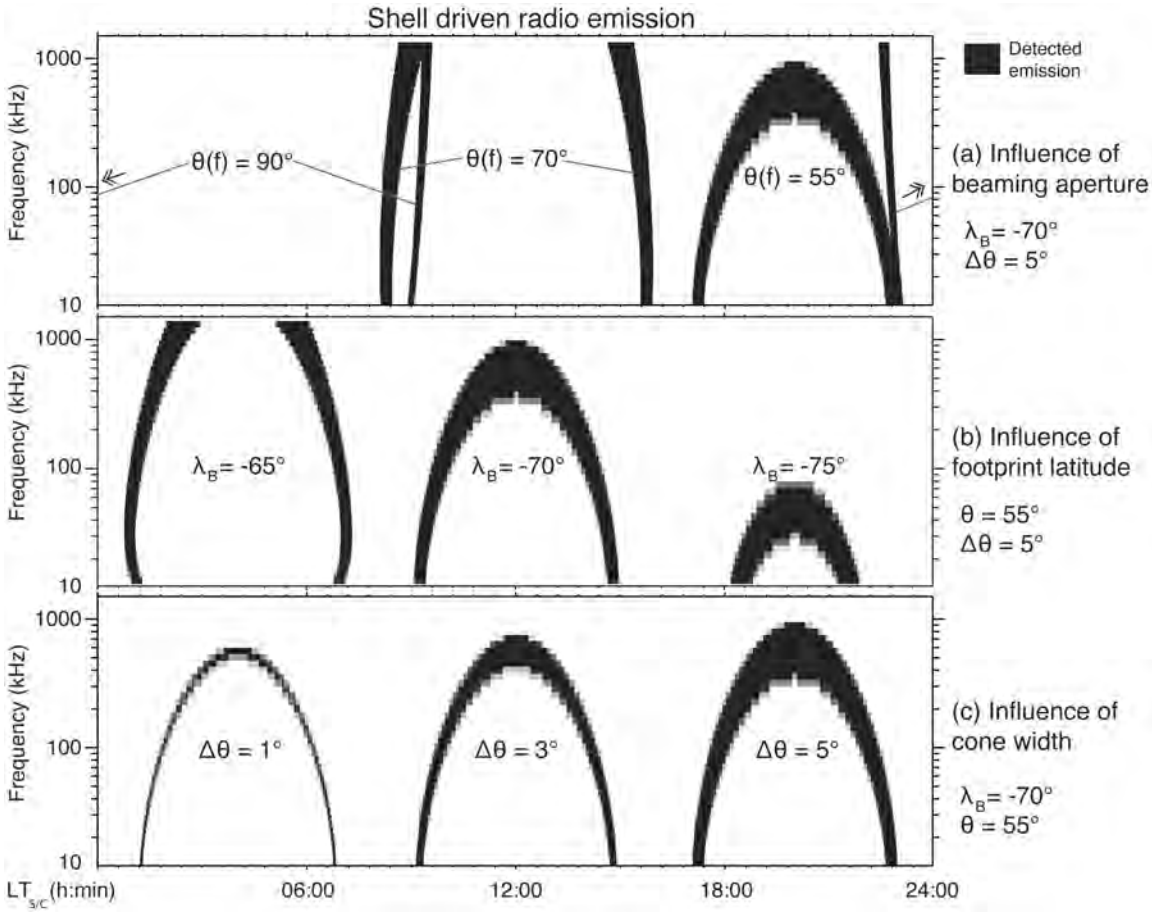

Figure A3. Same as Figure A2 but for shell-driven simulations. Arcs only appear for values of the beaming angle $\theta(f)$ ($\sim$55°), much lower than theoretically predicted values for shell electron distributions.

extent, beaming angle…) and consequently improve simulation results.

Appendix A: Parametric Study of Loss-Cone-/Shell-Driven Arcs Simulated With PRES

[34] Using both CMI loss-cone-/shell-driven simulations, we can simply simulate arcs generated by sources moving with respect to the observer. To estimate the influence of the parameters that most strongly affect the simulated arcs shape (see section 2), we present a parametric study for the simple case of a circular orbiter located in the equatorial plane (at 15 R_S) and observing southern sources fixed in LT as defined in Figure A1. Then, the influence of the source latitude λ_B, the beaming angle $\theta(f)$ and the cone thickness $\Delta\theta$ is investigated for loss-cone- (Figure A2) and shell- (Figure A3) driven simulations.

[35] As shown by Figure A2, loss-cone-driven simulations display clear concave arcs related to the decrease of the beaming angle θ at high frequencies. Both λ_B and v_{e-} strongly affect the arc morphology (width, thickness, high-frequency limit, concave shape at lowest frequencies), whereas $\Delta\theta$ essentially influences the arc thickness. Note that for each simulated arc, the visibility of its high-frequency limit is dependent on the distance between the planet and the observer.

[36] Figure A3 displays shell-driven simulations. An important result is shown on Figure A3a: a constant value of $\theta(f) = 90°$ leads to quasi-convex branches detected at 0200 and 1000 LT for a source located at 0400 LT. Strictly perpendicular emissions consequently do not allow to retrieve, even qualitatively, observed concave arcs (see Figures 1a and 1b). Further, oblique emissions using constant $\theta(f)$ lead to arcs qualitatively similar to the one observed for $\theta(f)$ as low as 55°. Then, Figures A3b and A3c show that similar to loss cone simulations, λ_B and $\Delta\theta$ differently affect the arc shape.

[37] We performed such a parametric study for each simulation detailed in sections 3 and 4, allowing us to derive the parameters that best fit the observed features (see Table 1).

[38] **Acknowledgments.** We thank the Cassini Radio Plasma and Wave Science (RPWS) engineers at the University of Iowa and N. Letourneur of the Laboratoire d'Etudes Spatiales et d'Instrumentation en Astrophysique (LESIA) for processing the data. We acknowledge support from the Centre National d'Etudes Spatiales (CNES).

[39] Wolfgang Baumjohann thanks the reviewers for their assistance in evaluating this paper.

References

Badman, S. V., S. W. H. Cowley, J.-C. Gérard, and D. Grodent (2006), A statistical analysis of the location and width of Saturn's southern aurora, *Ann. Geophys.*, *24*, 3533–3545.

Boischot, A., Y. Leblanc, A. Lecacheux, B. M. Pedersen, and M. L. Kaiser (1981), Arc structure in Saturn's radio dynamic spectra, *Nature*, *292*, 727–728.

Clarke, J. T., et al. (2005), Morphological differences between Saturn's ultraviolet aurorae and those of Earth and Jupiter, *Nature*, *433*, 717–719.

Connerney, J. E. P., M. H. Acuna, and N. F. Ness (1983), Currents in Saturn's magnetosphere, *J. Geophys. Res.*, *88*, 8779–8787.

Cowley, S., E. Bunce, and R. Prangé (2004a), Saturn's polar ionospheric flows and their relation to the main auroral oval, *Ann. Geophys.*, *22*, 1379–1394.

Cowley, S. W. H., E. J. Bunce, and J. M. O'Rourke (2004b), A simple quantitative model of plasma flows and currents in Saturn's polar ionosphere, *J. Geophys. Res.*, *109*, A05212, doi:10.1029/2003JA010375.

Davis, L. J., and E. J. Smith (1990), A model of saturn's magnetic field based on all available data, *J. Geophys. Res.*, *95*, 15,257–15,261.

Farrell, W. M., M. D. Desch, M. L. Kaiser, A. Lecacheux, W. S. Kurth, D. A. Gurnett, B. Cecconi, and P. Zarka (2005), A nightside source of Saturn's kilometric radiation: Evidence for an inner magnetosphere energy driver, *Geophys. Res. Lett.*, *32*, L18107, doi:10.1029/2005GL023449.

Galopeau, P., P. Zarka, and D. Le Queau (1989), Theoretical model of Saturn's kilometric radiation spectrum, *J. Geophys. Res.*, *94*, 8739–8755.

Galopeau, P. H. M., P. Zarka, and D. Le Quéau (1995), Source location of Saturn's kilometric radiation: The Kelvin-Helmholtz instability hypothesis, *J. Geophys. Res.*, *100*, 26,397–26,410.

Galopeau, P. H. M., M. Y. Boudjada, and H. O. Rucker (2004), Evidence of jovian active longitude: 1. Efficiency of cyclotron maser instability, *J. Geophys. Res.*, *109*, A12217, doi:10.1029/2004JA010459.

Gérard, J.-C., D. Grodent, J. Gustin, A. Saglam, J. T. Clarke, and J. T. Trauger (2004), Characteristics of Saturn's FUV aurora observed with the Space Telescope Imaging Spectrograph, *J. Geophys. Res.*, *109*, A09207, doi:10.1029/2004JA010513.

Grodent, D., J.-C. Gérard, S. W. H. Cowley, E. J. Bunce, and J. T. Clarke (2005), Variable morphology of Saturn's southern ultraviolet aurora, *J. Geophys. Res.*, *110*, A07215, doi:10.1029/2004JA010983.

Gurnett, D. A., et al. (2004), The Cassini radio and plasma wave investigation, *Space Sci. Rev.*, *114*, 395–463.

Hashimoto, K. (1984), A reconciliation of propagation modes of auroral kilometric radiation, *J. Geophys. Res.*, *89*, 7459–7466.

Hess, S., B. Cecconi, and P. Zarka (2008), Modeling of Io-Jupiter decameter arcs, emission beaming and energy source, *Geophys. Res. Lett.*, *35*, L13107, doi:10.1029/2008GL033656.

Kaiser, M. L., M. D. Desch, W. S. Kurth, A. Lecacheux, F. Genova, B. M. Pedersen, and D. R. Evans (1984), Saturn as a radio source, in *Saturn*, pp. 378–415, Univ. of Ariz. Press, Tucson.

Kaiser, M. L., P. Zarka, W. S. Kurth, G. B. Hospodarsky, and D. A. Gurnett (2000), Cassini and Wind stereoscopic observations of Jovian nonthermal radio emissions: Measurement of beam widths, *J. Geophys. Res.*, *105*, 16,053–16,062.

Lamy, L., P. Zarka, B. Cecconi, R. Prang, W. S. Kurth, and D. A. Gurnett (2008), Saturn kilometric radiation: Average and statistical properties, *J. Geophys. Res.*, *113*, A07201, doi:10.1029/2007JA012900.

Louarn, P., and D. Le Quéau (1996), Generation of the auroral kilometric radiation in plasma cavities-II. The cyclotron maser instability in small size sources, *Planet. Space Sci.*, *44*, 211–224.

Persoon, A. M., D. A. Gurnett, W. S. Kurth, and J. B. Groene (2006), A simple scale height model of the electron density in Saturn's plasma disk, *Geophys. Res. Lett.*, *33*, L18106, doi:10.1029/2006GL027090.

Queinnec, J., and P. Zarka (1998), Io-controlled decameter arcs and Io-Jupiter interaction, *J. Geophys. Res.*, *103*, 26,649–26,666, doi:10.1029/98JA02435.

Thieman, J. R., and M. L. Goldstein (1981), Arcs in Saturn's radio spectra, *Nature*, *292*, 728–731.

Treumann, R. A. (2006), The electron cyclotron maser for astrophysical application, *Astron. Astrophys. Rev.*, *13*, 229–315.

Warwick, J. W., et al. (1981), Planetary radio astronomy observations from Voyager 1 near Saturn, *Science*, *212*, 239–243.

Wu, C. S. (1985), Kinetic cyclotron and synchrotron maser instabilities—Radio emission processes by direct amplification of radiation, *Space Sci. Rev.*, *41*, 215–298.

Wu, C. S., and L. C. Lee (1979), A theory of the terrestrial kilometric radiation, *Astrophys. J.*, *230*, 621–626.

Xiao, F., L. Chen, H. Zheng, and S. Wang (2007), A parametric ray tracing study of superluminous auroral kilometric radiation wave modes, *J. Geophys. Res.*, *112*, A10214, doi:10.1029/2006JA012178.

Zarka, P. (1998), Auroral radio emissions at the outer planets: Observations and theories, *J. Geophys. Res.*, *103*, 20,159–20,194.

Zarka, P., B. Cecconi, and W. S. Kurth (2004), Jupiter's low-frequency radio spectrum from Cassini/Radio and Plasma Wave Science (RPWS) absolute flux density measurements, *J. Geophys. Res.*, *109*, A09S15, doi:10.1029/2003JA010260.

B. Cecconi, S. Hess, L. Lamy, R. Prangé, and P. Zarka, LESIA, Observatoire de Paris, 5 Place Jules Janssen, F-92190 Meudon, France. (laurent.lamy@obspm.fr)